The Astrophysical Journal, 977:167 (12pp), 2024 December 20 https://doi.org/10.3847/1538-4357/ad90bd

On the Origins, Remnant, and Multimessenger Prospects of the Compact Binary Merger GW230529

Koustav Chandra[1], Ish Gupta[1], Rossella Gamba[1,2], Rahul Kashyap[1], Debatri Chattopadhyay[3], Alejandra Gonzalez[4], Sebastiano Bernuzzi[4], and B. S. Sathyaprakash[1,3,5]
[1] Institute for Gravitation & the Cosmos and Physics Department, The Pennsylvania State University, University Park, PA 16802, USA; kbc595@psu.edu
[2] Department of Physics, University of California, Berkeley, CA 94720, USA
[3] School of Physics and Astronomy, Cardiff University, Cardiff, CF24 3AA, UK
[4] Theoretisch-Physikalisches Institut, Friedrich-Schiller-Universität Jena, 07743, Jena, Germany
[5] Department of Astronomy and Astrophysics, Penn State University, University Park, PA 16802, USA
Received 2024 May 14; revised 2024 October 31; accepted 2024 November 7; published 2024 December 11

Abstract

This study investigates the origins of GW230529, delving into its formation from massive stars within isolated binary systems. Utilizing population-synthesis models, we present compelling evidence that the neutron star component forms second. However, the event's low signal-to-noise ratio introduces complexities in identifying the underlying physical mechanisms driving its formation. Augmenting our analysis with insights from numerical relativity, we estimate the final black hole mass and spin to be approximately $5.3\,M_{\odot}$ and 0.53, respectively. Furthermore, we employ the obtained posterior samples to calculate the ejecta mass and kilonova light curves resulting from *r*-process nucleosynthesis. We find the ejecta mass to be within 0–$0.06\,M_{\odot}$, contingent on the neutron star equation of state. The peak brightness of the kilonova light curves indicates that targeted follow-up observations with a Rubin-like observatory may have detected this emission.

Unified Astronomy Thesaurus concepts: Gravitational wave astronomy (675); Neutron stars (1108)

1. Introduction

Electromagnetic observations have played a pivotal role in constraining the mass spectra of neutron stars (NSs) and black holes (BHs). Notably, X-ray and radio observations have consistently indicated that the maximum masses of NSs fall within the range of 2–$2.6\,M_{\odot}$, while BH masses have been found to exceed $5\,M_{\odot}$ (C. D. Bailyn et al. 1998; F. Ozel et al. 2010; W. M. Farr et al. 2011; J. Antoniadis et al. 2016; J. Alsing et al. 2018; W. M. Farr & K. Chatziioannou 2020; E. Fonseca et al. 2021; R. W. Romani et al. 2022). Consequently, these detections have implied a notable absence of compact binaries within the mass range of 2.6–$5\,M_{\odot}$, a notion reinforced by initial gravitational-wave (GW) observations (B. P. Abbott et al. 2019a; R. Abbott et al. 2021). However, supernova (SN) simulations have predicted the existence of BHs within this gap (C. L. Fryer et al. 2012). Furthermore, the recent observation of the binary merger GW230529_181500 (hereafter referred to as GW230529) has provided conclusive evidence for the existence of compact objects within this mass range (Ligo Scientific Collaboration et al. 2024, hereafter LVK).

This event was observed only in LIGO Livingston (J. Aasi et al. 2015), with a signal-to-noise ratio (SNR) $\gtrsim 11$ and a low false-alarm rate of less than one event per thousand years by the PyCBC offline analysis. Assuming GW230529 is the result of the merger of a black hole–neutron star (BHNS) binary on a quasi-circular orbit, the data are consistent with the merger of two compact objects with masses $3.6^{+0.8}_{-1.2}\,M_{\odot}$ and $1.4^{+0.6}_{-0.2}\,M_{\odot}$ (90% credible intervals), making it the most symmetric mixed-compact-binary merger detected via GWs.

Measuring these mass parameters is part of the inverse problem. Other parameters of astrophysical interest include, but are not limited to, the components' spins, the tidal properties, and the remnant properties. A Bayesian inference approach is typically employed, which necessitates model evaluations to reliably infer the posterior distribution for the parameters that characterize the observed signal (J. Veitch & A. Vecchio 2010; E. Thrane & C. Talbot 2019). While the data containing GW230529 were matched against several state-of-the-art GW signal models, LVK's initial analysis assumed priors that are effectively flat in component masses, spin magnitudes, and isotropic spin orientations. These astrophysically agnostic priors do not provide information about GW230529's possible formation mechanism.

Therefore, LVK reweighed the posterior samples using a few astrophysically informed mass and spin distributions to constrain the source properties (M. Fishbach et al. 2020; S. Biscoveanu et al. 2022; A. Farah et al. 2022; A. Ray et al. 2023). For instance, the study revealed that the phenomenological population-informed prior, "Power Law + Dip + Break," predicts significantly different component masses than uninformed priors. This demonstrates the substantial impact that prior choice can have on the inferred masses and spins of the GW230529 source. The observed differences are consistent with the model's preference for mass-symmetric systems, especially considering the event's low SNR.

Also, the employed astrophysically informed priors are phenomenological and contain only an observationally constrained understanding of stellar and binary evolution. Further, J.-P. Zhu et al. (2024) found that GW230529's masses are close to those predicted in their BHNS binary population simulations.

In this article, we reanalyze the data containing GW230529 with population-informed priors to provide conclusive insights into the probable physical processes underlying this binary formation.

Leading formation models of GW230529-like systems include the isolated evolution of massive binary stars in galactic fields via the common envelope (CE) and the dynamical assembly aided by either a tertiary companion, multiple exchanges in dense clusters, or gas-assisted migration (see I. Mandel & F. S. Broekgaarden 2022 and references therein). While direct collapse leading to the formation of the primary component is unlikely due to its low mass, recent population-synthesis models have argued in favor of the plausibility of such systems arising from isolated evolution scenarios (F. S. Broekgaarden & E. Berger 2021; F. S. Broekgaarden et al. 2021; D. Chattopadhyay et al. 2021; D. Chattopadhyay et al. 2022). However, these models have major uncertainties such as mass loss, mass transfer, and the impact of SN explosions, resulting in a broad spectrum of merger-rate predictions and varying mass and spin distributions.

We describe our methodology in Section 2, utilizing it subsequently in Section 3.1 to ascertain the nature of the merger—specifically, whether the NS or BH formed first. Consequently, in Section 3.2, we employ the evidence ratio of posterior samples and the distribution of log-likelihood ratios to distinguish between various formation models, shedding light on the most likely formation mechanism of GW230529.

We then use the posterior samples corresponding to these models to analyze the characteristics of the remnant BH, as detailed in Section 4.1. Our analysis is conducted using a selection of equations of state (EOSs) that adhere to current astrophysical and nuclear constraints (M. Breschi et al. 2024). Furthermore, this section assesses the probability of NSs' tidal disruption during the merger.

Subsequently, in Section 4.2, we present the range of ejecta masses that inform the *r*-process synthesis resulting from such events. Our analysis incorporates four fiducial EOSs, namely `APR4` (A. Akmal et al. 1998), `SLy` (E. Chabanat et al. 1998; F. Douchin & P. Haensel 2001), `DD2` (M. Hempel & J. Schaffner-Bielich 2010; S. Typel et al. 2010), and `H4` (N. Glendenning & S. Moszkowski 1991; B. D. Lackey et al. 2006; J. S. Read et al. 2009).

Finally, in Section 4.3, we compute the light curves associated with kilonovae (KNe) for the event under consideration. While these light curves may be fainter compared to those observed in the GW170817 event, they may be detectable through targeted searches using observatories such as the Rubin Observatory (Z. Ivezić et al. 2019). Last, in Section 5, we conclude our findings.

2. Methods

We infer GW230529's properties by analyzing 128 s of LIGO Livingston data using the Bayesian parameter estimation (PE) library `BILBY` (G. Ashton et al. 2019) and the posterior sampling algorithm `DYNESTY` (J. S. Speagle 2020). We assume a noise power spectrum given by the median estimate provided by `BAYESLINE` (T. B. Littenberg & N. J. Cornish 2015) and use frequencies in the range of 20–1792 Hz for evaluating the GW transient log-likelihood ratio $\ln \mathcal{L}$. Furthermore, to speed up the likelihood evaluation, we include heterodyning (also known as relative binning; N. J. Cornish 2010, 2021; B. Zackay et al. 2018; K. Krishna et al. 2023). For our analysis, we use the quasi-circular frequency-domain phenomenological waveform model `IMRPhenomNSBH` (F. Foucart et al. 2013, 2014; S. Khan et al. 2016; T. Dietrich et al. 2019; J. E. Thompson et al. 2020). This waveform approximant models signals using the dominant (quadrupole) harmonic and is specifically designed to model GWs emanating from BHNS binary mergers with mass ratios ranging from equal mass up to $q = m_{\rm BH}/m_{\rm NS} = 15$. It also incorporates BH spins up to a dimensionless value of $\chi_{\rm BH} = 0.5$ and includes matter effects through tidal parameters $\Lambda_{\rm NS}$ ranging from 0 to 5000. We assess the impact of waveform systematics in Appendix A, finding them to be negligible for the purposes of our study.

However, unlike the original analyses, we exclude the marginalization over the systematic error in the measured astrophysical strain due to the detector calibration. This error is subdominant to the systematic errors from waveform modeling and prior choices, and we therefore neglect it (G. Ashton & T. Dietrich 2022). Furthermore, as discussed in Section 3.2, we apply astrophysically motivated mass and spin priors while using uninformative priors for all other parameters. It is important to note that, for all our analyses, we utilize the BH and NS masses viz $m_{\rm BH}$ and $m_{\rm NS}$ priors derived from population-synthesis models as two distinct, one-dimensional independent priors.

While various assumptions may be made to model the formation pathway of this system, one needs to determine the relative probability of two models (in this case, binary formation processes) given the data. The Bayesian evidence, $\mathcal{Z}$, quantifies this support. Varying prior assumptions can yield differing parameter estimates; therefore, the Bayes factor, $\mathrm{BF}^A_B = \mathcal{Z}_A/\mathcal{Z}_B$, indicates whether the prior assumption A is favored or disfavored compared to B based on the data. This comparison is particularly crucial as strong prior assumptions may bias the posteriors toward potentially arbitrary values at the expense of the evidence. Furthermore, we also compare the log-likelihood ratio distribution since certain models allow for broader priors and incur a higher Ockham penalty.

3. Astrophysical Implications

LVK found no conclusive evidence either supporting or refuting the presence of tidal effects in the GW230529 signal. This makes it difficult to determine the nature of the compact objects involved. However, they showed that the (lighter) secondary component appears to be an NS, while the (heavier) primary is likely a BH, when using observationally constrained priors. In this section, we investigate which of the binary components formed first and determine their formation mechanism.

3.1. BHNS or NSBH?

BHNS binaries can generally be divided into two categories: (1) BHNS mergers, where the BH forms first, and (2) neutron star–black hole (NSBH) mergers, in which the NS forms first. While BHNSs are the dominant binaries according to population-synthesis studies (D. Chattopadhyay et al. 2021), NSBHs are more exciting as they can form radio pulsars, generate KNe (C. Barbieri et al. 2020), and lead to precise measurement of NS spins (I. Gupta 2024). To discriminate between the two, we analyze GW230529 using different predicted distributions of the detectable BHNS and NSBH masses and spins for different metallicity choices ($Z = 0.02$, 0.001, 0.005, 0.0005) from the base model of D. Chattopadhyay et al. (2022). These models are expected to be representative of the population of such binaries obtained from GW observations.

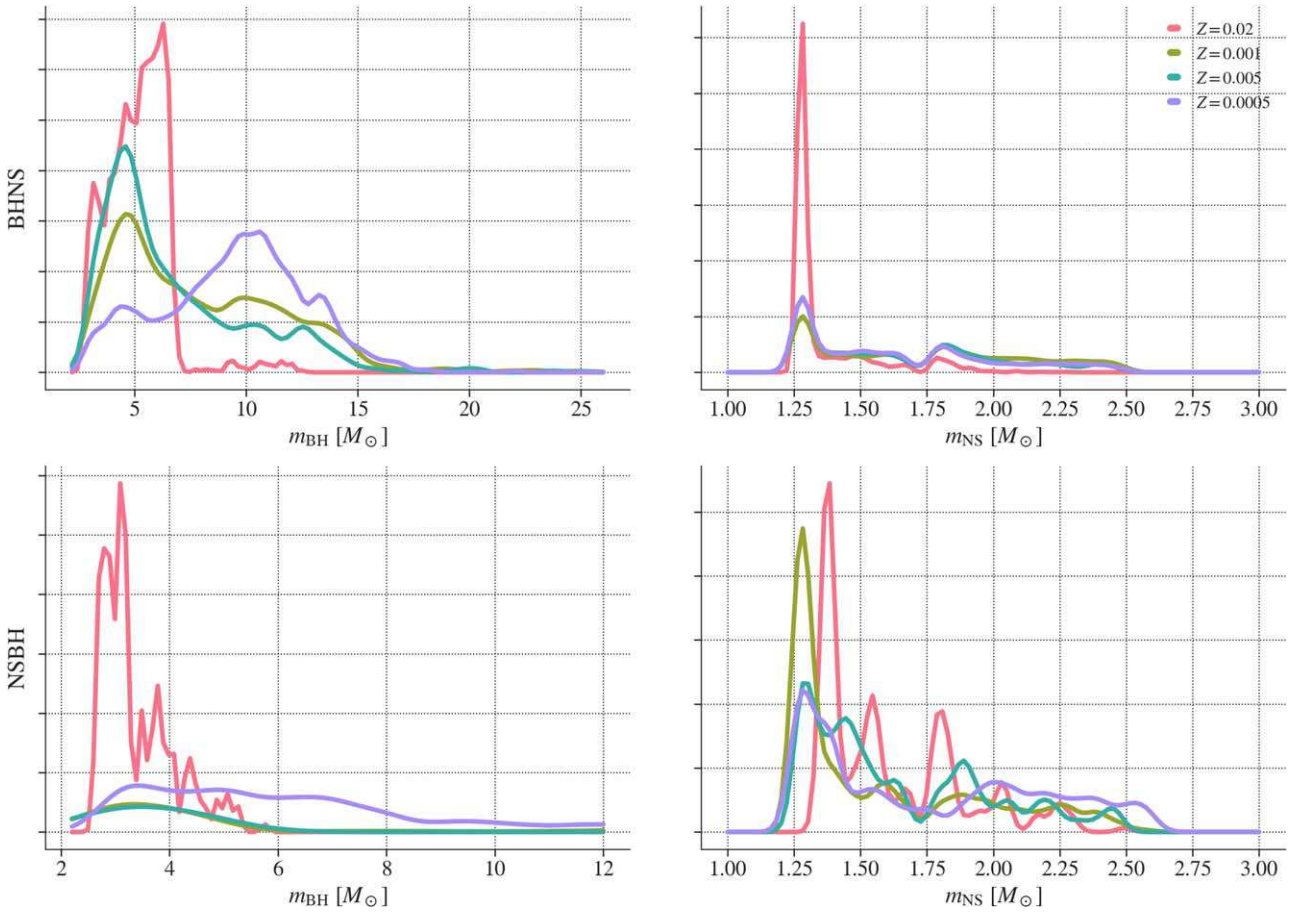

Figure 1. Predicted component mass distributions for BHNS (top panel) and NSBH systems (bottom panel) across varying subsolar metallicities, as outlined in D. Chattopadhyay et al. (2021). As can be observed, NSBH systems tend to produce binaries with lighter BHs across different metallicities.

As can be seen in Figure 1, the BHNS (top panel) and NSBH (bottom panel) systems exhibit distinct mass spectra, with BHs in BHNS systems being more massive. This is because the heavier star evolves faster and remains massive enough to form a BH even after the mass transfer (J. R. Hurley et al. 2000; K. Belczynski et al. 2010). In contrast, NSBH systems have more mass-symmetric progenitors, and more so at higher metallicities. The heavier star transfers enough mass to its companion to form an NS, whereas its companion becomes a BH. However, at lower metallicities, reduced stellar winds lead to reduced mass loss, creating larger BHs that merge over a shorter timescale (J. R. Hurley et al. 2000).

We use BH spins derived from fits in D. Chattopadhyay et al. (2021) for NSBH mergers but restricted to $\chi_{\rm BH} = 0.5$ as `IMRPhenomNSBH` is not calibrated for $\chi_{\rm BH} > 0.5$. Moreover, attaining spins greater than this would require an unphysical amount of matter accretion (I. Mandel & T. Fragos 2020). Although tidal synchronization can lead to higher BH spins, the fraction of such binaries is small (D. Chattopadhyay et al. 2021). For the BHNS case, we set $\chi_{\rm BH} = \chi_{\rm NS} = 0$ as the rotational velocities of NSs are anticipated to diminish over time due to electromagnetic radiation (T. Fragos & J. E. McClintock 2015; L. Ma & J. Fuller 2019). As ground-based GW observatories are only expected to detect these binaries close to the merger, we assume that the BH and NS objects have negligible spin. Thus, for the second analysis, we effectively assume that the source of GW230529 is a nonspinning BHNS binary. This is because the efficiency of angular momentum transfer in BH progenitors is crucial for determining the spin characteristics of the resultant BH. In the dominant evolutionary scenarios involving helium (He) stars, efficient angular momentum transfer from core to envelope typically results in most of the He star's core becoming nonspinning and hence the final BH (Y. Qin et al. 2018; S. S. Bavera et al. 2020). In an NSBH system, however, the first-formed compact object (an NS in this case), if sufficiently close and massive, can induce tidal interactions that potentially spin up the second-born BH at birth.

Figure 2 shows an obvious trend; the log-likelihood ratio distribution associated with the BHNS (top panel) has a higher median log-likelihood ratio value and contains a prominent peak compared to the NSBH case (bottom panel) for the same metallicity choices. Further, the BHNS hypothesis is preferred with a $\ln {\rm BF}^{\rm BHNS}_{\rm NSBH} > 17(9)$ for a metallicity choice of $Z = 0.02$ (0.0005). Therefore, we will assume that GW230529 is a BHNS merger for the remainder of the paper. Note that our results are robust against waveform systematics (see Appendix A).

3.2. Constraints on Binary Evolution

The pathway leading to BHNS mergers is still debated. The prevailing hypothesis suggests that these mergers arise from two massive stars that were born in a binary and evolved in isolation, typically involving the CE episode that tightens the binary's orbit (I. Mandel & F. S. Broekgaarden 2022; see Figure 3). However, accurately estimating the rates of these mergers is challenging for several reasons.

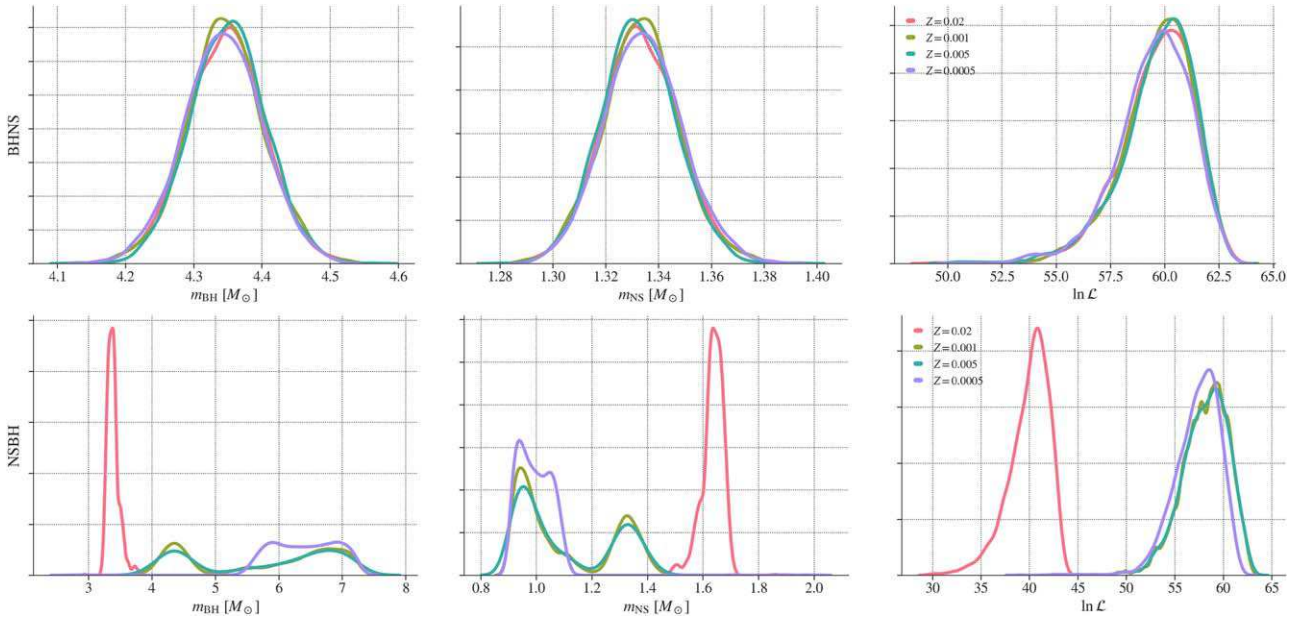

Figure 2. Posterior densities for the mass of GW230529 as inferred using the population-inspired BHNS (top panel) and NSBH (bottom panel) priors described in Section 3.1. In the right-hand column, we include the log-likelihood ratio distribution.

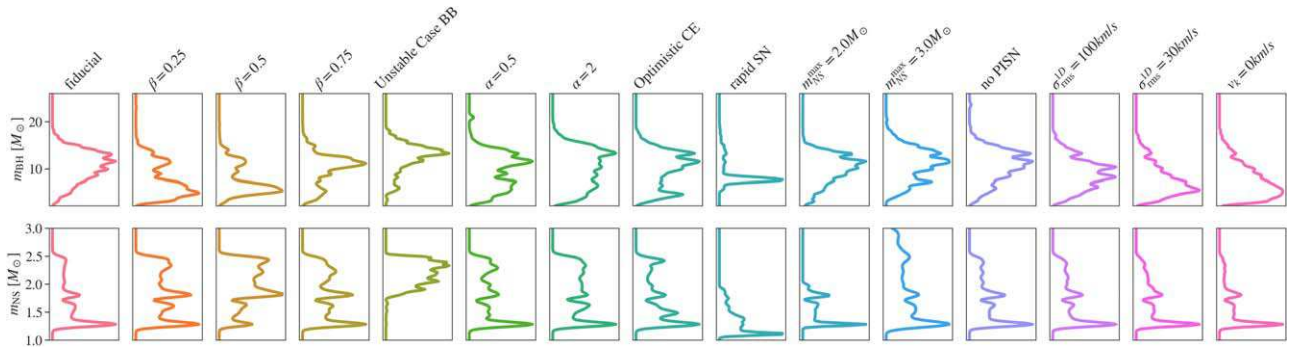

Figure 3. Predicted BHNS component mass distributions. Each row shows the 15 different population-synthesis variations used by F. S. Broekgaarden et al. (2021).

First, the physical processes that govern the evolution of massive binary-star systems, including the dynamics of the CE phase (N. Ivanova et al. 2013), mass-transfer efficiency between binary components, and the kicks imparted to stars during SNe, are complex and poorly understood, leading to considerable uncertainty (K. Belczynski et al. 2022). Second, uncertainties arise due to the star formation rate and the metallicity distribution within star-forming gas across cosmic time (D. Langeroodi et al. 2023; A. M. Garcia et al. 2024). Together, they significantly impact the detectable BHNS mass distributions.

Since we are interested in determining the physical process leading to GW230529's formation, we only focus on the uncertainties related to the physical processes. To that end, following F. S. Broekgaarden et al. (2021), we assumed 15 different binary population-synthesis predictions for BHNS mass distribution. These models implement variations to the fiducial model in different aspects of physics relevant to the binary evolution, such as mass-transfer efficiency between binary components and the kicks imparted to the stars. We briefly summarize them below.

The $\beta=0.25$, 0.5, and 0.75 models assume fixed mass-transfer efficiencies. These models represent the fraction of mass lost by the donor star that its companion accretes. On the other hand, the "unstable case BB" model involves an unstable mass-transfer phase from a stripped post-helium-burning star onto a BH.

For the $\alpha=0.5$ and 2 models, a pessimistic CE scenario is assumed, where the donor stars struggle to successfully eject their envelopes, resulting in efficiency parameters of 0.5 and 2, respectively. Conversely, the "optimistic" CE scenario posits that these systems can survive such challenges.

To avoid creating a remnant mass gap between NSs and BHs, which contradict observations from X-ray binaries, F. S. Broekgaarden et al. (2021) use a delayed remnant mass prescription in their simulations. However, the "rapid SNe" model adopts a faster remnant mass prescription and is consistent with current observations.

The models labeled as $m_{\rm NS}^{\rm max}=2M_\odot$ and $m_{\rm NS}^{\rm max}=3M_\odot$ set the maximum mass of NSs to 2 and $3\,M_\odot$, respectively. It is worth noting that the latter case may be considered unrealistic since the maximum mass supported by current EOSs for nonrotating NSs is $\lesssim 2.9\,M_\odot$ (D. A. Godzieba et al. 2021).

The "no PISN" prescription excludes the pair-instability process responsible for the scarcity of first-generation BHs with masses between 65 and $120\,M_\odot$. Additionally, the $\sigma_{\rm cc}=30\,{\rm km\,s^{-1}}$ and $\sigma_{\rm cc}=100\,{\rm km\,s^{-1}}$ prescriptions explore variations of natal kicks compared to the one-dimensional rms

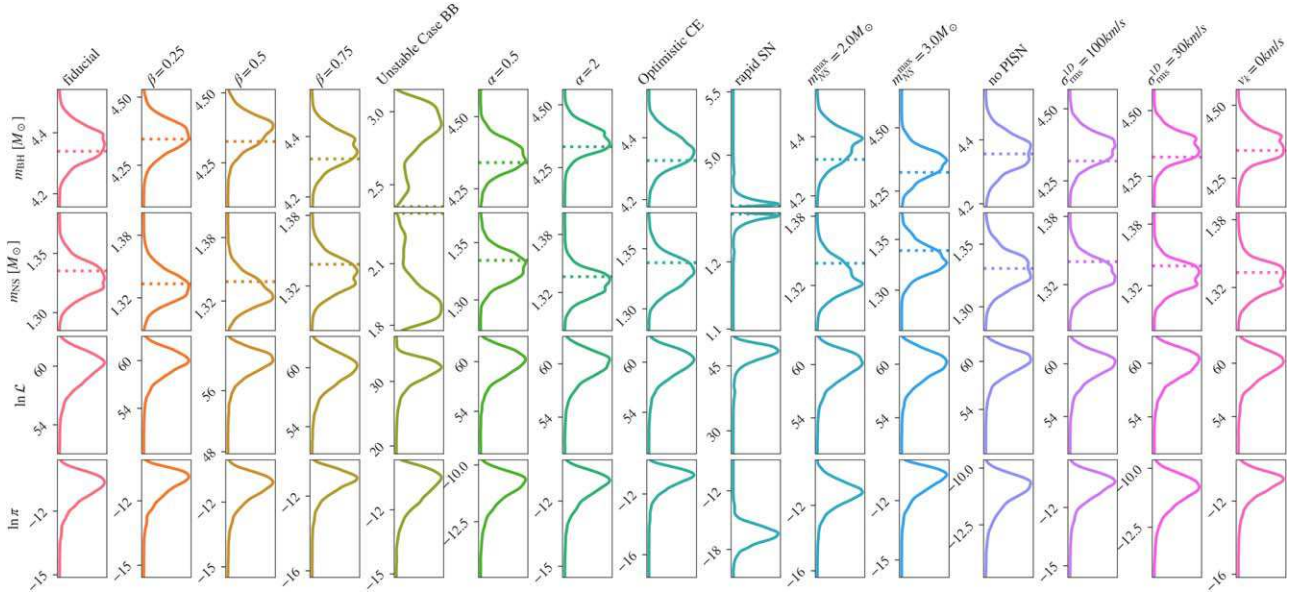

Figure 4. Posterior densities for the mass of GW230529 under different binary evolution assumptions. We also include the distributions of the log-likelihood and log-prior of the posterior samples. The dotted lines in the first two rows denote the maximum-likelihood estimates of $m_{\rm BH}$ and $m_{\rm NS}$, respectively.

velocity dispersion of $\sigma_{\rm cc} = 265\,{\rm km\,s^{-1}}$ used in the fiducial model. These lower values can occur in ultrastripped SNe and electron-capture SNe, leading to reduced binary disruption. Finally, the $v_{\rm k,BH} = 0\,{\rm km\,s^{-1}}$ assumption posits that BHs receive no SN natal kicks.

Figure 4 summarizes our findings when assuming these populations. We observe that, except for the "unstable case BB" and "rapid SNe" models, the inferred posteriors are largely in agreement with each other. This alignment was anticipated, given that these two population models restrict the BH mass to a range outside the support for this signal. Moreover, we do not observe any trends in the log-prior distribution for the other models, which indicates that all the information about the evidence for and against binary evolution is contained in the distribution of the log-likelihood ratio. However, we also do not observe any differences in the shape and location of the log-likelihood ratio distribution, indicating that all models are equally likely. In fact, the $\ln {\rm BF}^{S}_{N}$ for all analyses, except for the "unstable case BB" and "rapid SNe" models, is approximately $63. \pm 0.15$. This suggests that the outputs of these analyses are statistically equivalent. The "unstable case BB" and "rapid SNe" models have $\ln {\rm BF}^{S}_{N}$ values of 37.0 and 51.87, respectively, indicating they are less favored. This is because these priors prevent exploration of the higher-likelihood region.

This is not surprising since the signal's SNR is low. Finally, it is noteworthy that, for the majority of our analysis, we determine the BH and NS masses to be $m_{\rm BH} = 4.3^{+0.08}_{-0.09}\,M_\odot$ and $m_{\rm NS} = 1.4^{+0.02}_{-0.02}\,M_\odot$, respectively, while finding that the $\ln {\rm BF}^{\rm fiducial}_{\rm pop-agnostic} \sim 1$.

4. Multimessenger Predictions

4.1. Remnant Properties

Assuming GW230529 is a BHNS merger, estimates of the final mass and spin of the remnant BH can be made using the models of F. Zappa et al. (2019) and A. Gonzalez et al. (2023). Rather than employing the uninformative posteriors on the tidal parameters obtained from our PE, we combine samples obtained using the the `IMRPhenomNSBH` waveform with the EOSs of M. Breschi et al. (2024). This set was obtained by performing joint analysis of GW170817 (B. P. Abbott et al. 2017, 2019b) and AT2017gfo (V. A. Villar et al. 2017), including information from numerical relativity (NR) in the KN model employed and folding in pulsar mass and radius measurements (M. C. Miller et al. 2021; R. W. Romani et al. 2022; S. Vinciguerra et al. 2024).

Figure 5 shows the predicted remnant property distribution for various formation-model assumptions. We find that all models, with the exception of the "unstable case BB" and "rapid SNe," predict the formation of a $M_f = 5.3^{+0.1}_{-0.1}\,M_\odot$ BH remnant, with a dimensionless spin $a_f = 0.53^{+0.01}_{-0.01}$. We have checked that these values are weakly dependent on the EOS choice.

Applying the classification proposed in Section II of A. Gonzalez et al. (2023), we further find high probability ($\geqslant$99%) of the NS being at least partially tidally disrupted during the coalescence, with about 13% probability of such disruption happening far from the system's innermost circular orbit. This value is consistent with the findings of LVK, indicating that one would expect to observe a suppressed but nonetheless present ringdown signal and a possible electromagnetic counterpart.

4.2. Ejecta Mass

During a BHNS merger, the NS can get tidally disrupted. The neutron-rich ejecta from such disruption can emit KNe (B. D. Metzger 2017), provided the NS disrupts before it enters the innermost circular orbit ($R_{\rm ISCO}$) corresponding to the BH. If the NS sheds mass after crossing this orbit, the BH swallows the ejecta, producing no KNe. Hence, the distance at which the NS starts shedding mass must be greater than $R_{\rm ISCO}$ to produce a transient. The ratio of the mass-shedding radius and $R_{\rm ISCO}$ increases with the BH spin and decreases with the binary's mass ratio and the NS's compactness for aligned spin. For antialigned cases, the mass-shedding limit increases significantly, disfavoring tidal disruption. Thus, mass-symmetric binaries with a rapidly spinning BH are conducive to generating KNe. Similarly, less compact NSs (coming from stiff EOSs) are easier to disrupt for aligned spin cases, which is also favorable for KN

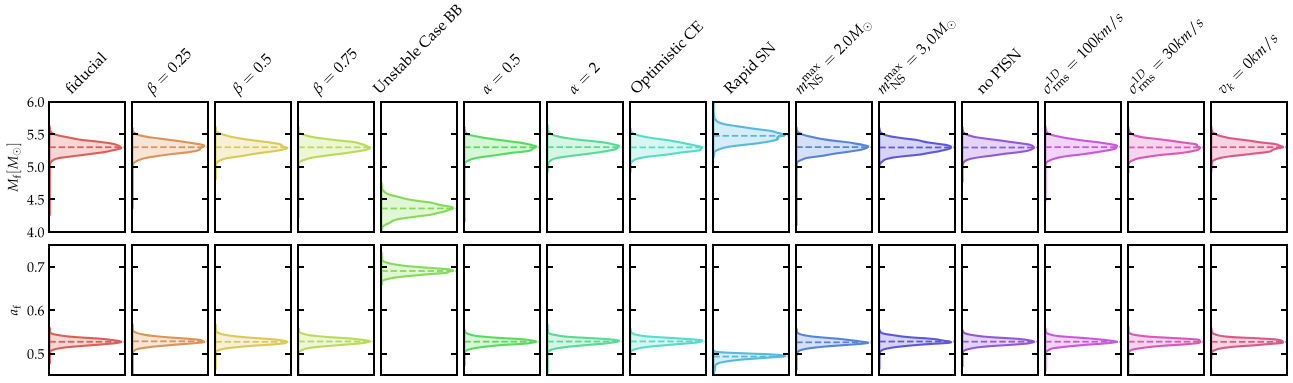

Figure 5. Posterior densities for the remnant BH mass and spin under different binary evolution assumptions. These quantities are computed from NR fits of BHNS binaries using the posteriors from Section 3.2 and the EOS information coming from multimessenger analyses of GW170817 and AT2017gfo. For most of the scenarios considered, we find $M_f = 5.3^{+0.1}_{-0.1}\,M_\odot$ and $a_f = 0.53^{+0.01}_{-0.01}$.

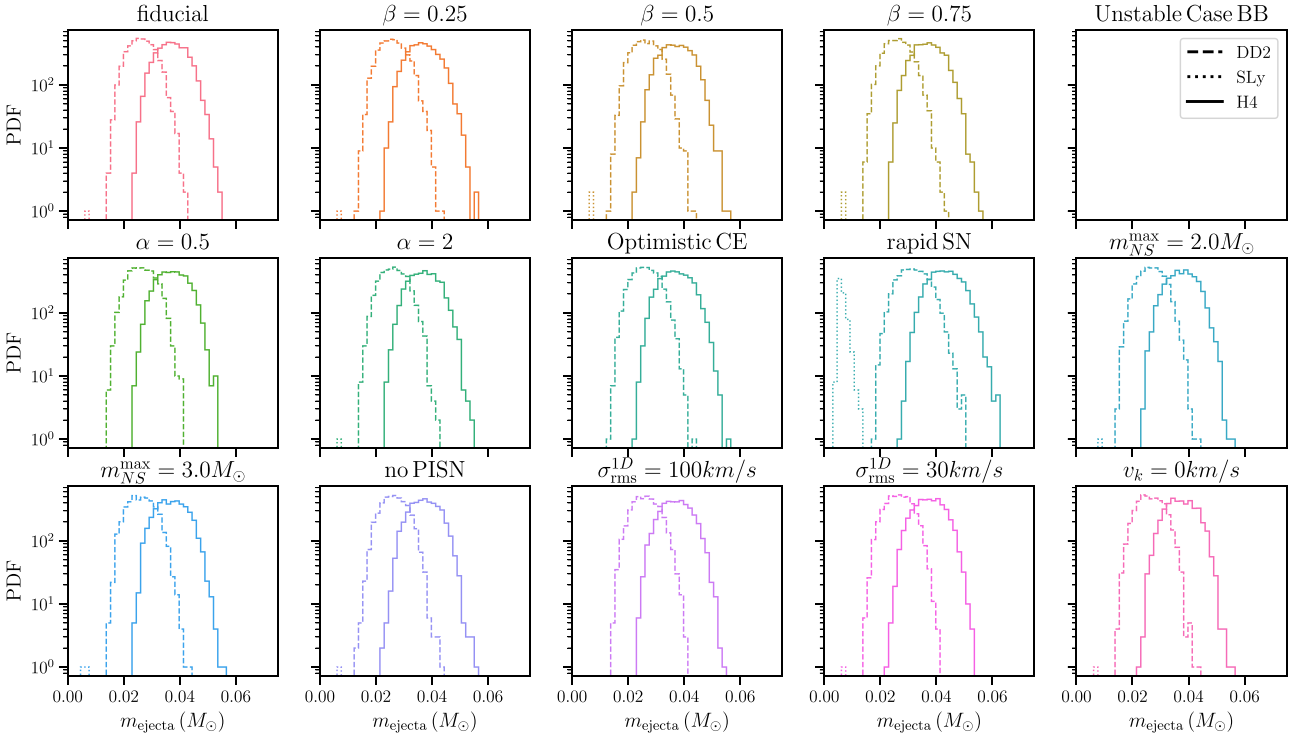

Figure 6. The probability density function (PDF) for the total ejecta mass for different EOSs and corresponding to the various population models. No ejecta was obtained for the APR4 EOS.

production. We utilize the isotropic framework proposed in W. D. Arnett (1980), D. Arnett (1982), E. Chatzopoulos et al. (2012), V. A. Villar et al. (2017), R. Kashyap et al. (2019), and I. Gupta et al. (2024, in preparation) to calculate KN light curves resulting from *r*-process nucleosynthesis in BHNS mergers (see K. Kawaguchi et al. 2024 for comparison and angle dependence on light curves). The KN light curves are characterized by the ejecta mass, velocity, and opacity, which are informed by and related to the binary parameters using up-to-date NR simulations (J. M. Lattimer & D. N. Schramm 1974, 1976; K. Kyutoku et al. 2018, 2021; C. Barbieri et al. 2019; C. J. Krüger & F. Foucart 2020a). We use the posterior samples obtained in Section 3.2 and calculate the mass of total ejecta, dynamical ejecta, and unbound disk ejecta using the fits from C. J. Krüger & F. Foucart (2020b) and G. Raaijmakers et al. (2021).

This calculation is performed using four different EOSs: APR4 (A. Akmal et al. 1998), SLy (E. Chabanat et al. 1998; F. Douchin & P. Haensel 2001), DD2 (M. Hempel & J. Schaffner-Bielich 2010; S. Typel et al. 2010), and H4 (N. Glendenning & S. Moszkowski 1991; B. D. Lackey et al. 2006; J. S. Read et al. 2009; see Figure 10 in Appendix B for corresponding mass–radius curves). Among these, APR4 and SLy give relatively more compact NSs, whereas DD2 and H4 result in less compact ones. Thus, the latter two will produce more ejecta than the former. We find that APR4 does not give any ejecta for samples corresponding to any population models. Figure 6 shows the probability distribution of total ejecta for the remaining three EOSs. Across population models, the total ejecta mass corresponds to SLy $\lesssim 0.01\,M_\odot$, DD2 $\lesssim 0.05\,M_\odot$, and H4 $\lesssim 0.07\,M_\odot$. Most ejecta are produced for the samples corresponding to the "rapid SNe" population model, which is due to its preference for a more

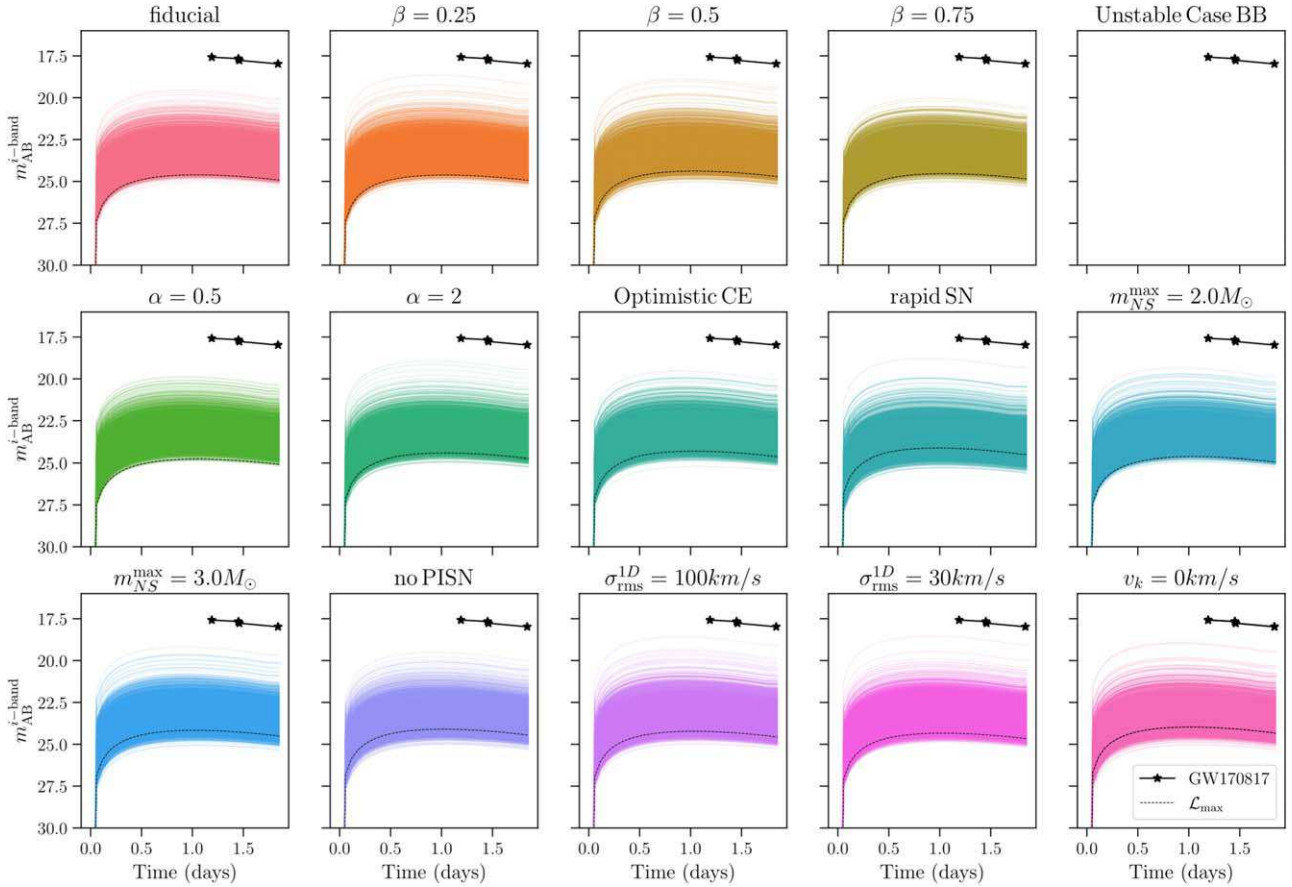

Figure 7. KN light curves in the *i* band corresponding to the different population models for the H4 EOS. The dotted line shows the light curve associated with the maximum-likelihood parameter estimates for each model.

symmetric binary (cf. Figure 4). On the other hand, the "unstable case BB" population model results in no ejecta due to its preference for more massive (hence more compact) NSs. Note that both "rapid SNe" and "unstable case BB" population models are disfavored compared to others, as discussed in Section 3.2. We obtain similar results when employing the EOSs from M. Breschi et al. (2024), with a distribution of ejecta masses peaking between SLy and DD2.

4.3. Kilonova Light Curves

Choosing the most optimistic scenarios, namely those corresponding to the H4 EOS, we calculate the bolometric KN light curves (see Appendix B for DD2). We convert them to bandwise light curves for the *ugrizy* filters (see I. Gupta et al. 2023 and Appendix B for more details). Figure 7 shows *i*-band curves together with the curve for maximum-likelihood ($\mathcal{L}_{\max}$) binary parameters. We also compare the points from the detected light curve of GW170817 (J. Guillochon et al. 2017; V. A. Villar et al. 2017) in the *i*-band.

From Figure 7, we note that only the "unstable case BB" mass-transfer population model does not support a KN after the merger—a population model disfavored by our analysis. For all other population models, the KN is expected to be considerably dimmer than the one observed for GW170817. This is expected, given that the KN flux is inversely proportional to the distance squared and that GW230529 is located approximately 5 times farther than GW170817 LVK. For all population models, the curves corresponding to the $\mathcal{L}_{\max}$ binary parameters prefer comparatively dimmer KNe, which is because the $\mathcal{L}_{\max}$ parameters correspond to a more mass-asymmetric binary located farther away. These results are identical when considering the EOSs from M. Breschi et al. (2024).

Focusing on the KN properties, we note that the luminosity in the *i*-band peaks 1 day after the merger for all population models except "unstable case BB." The peak luminosities corresponding to the $\mathcal{L}_{\max}$ binary parameters lie in the range [23.97, 24.67] mag. For the "fiducial" population model and $\mathcal{L}_{\max}$ binary parameters, Table 1 shows the bandwise peak luminosities and their decay. The latter is the absolute difference between the peak luminosity and 1 day after it.

To gauge the KN detectability, we compare the peak luminosity in each band with the corresponding limiting magnitude ($m_{\rm RO}^{\rm lim}$) of the Rubin Observatory for a single, 30 s long exposure. While the KNe in the *y* band are the brightest, Rubin would not have observed this owing to its relatively poor sensitivity in this band. For the "fiducial" population model, peak luminosities in the *gri* bands come closest to the limiting magnitude threshold. However, a targeted observation with 600 s exposure increases the limiting magnitude for the *g* and *i* bands to 26.62 and 25.62 (I. Gupta 2023; M. Branchesi et al. 2023), respectively, making the KNe visible in these bands.

5. Conclusions

In this work, we have studied the origins of GW230529, assuming that it is a binary formed via the classical isolated

Table 1
The (Optical) Bandwise Peak Luminosities and Decay in Luminosity 1 Day After Peak for KNe with $\mathcal{L}_{\max}$ Binary Parameters Corresponding to the "Fiducial" Population Model and the H4 EOS

Band	$m_{\rm RO}^{\rm lim}$ ($m_{\rm AB}$)	Peak ($m_{\rm AB}$)	Decay ($m_{\rm AB}$)
u	23.9	26.63	1.85
g	25.0	25.80	1.04
r	24.7	25.05	0.59
i	24.0	24.61	0.35
z	23.3	24.27	0.16
y	22.1	24.04	0.10

Note. For comparison, the single-exposure (30 s) bandwise limiting magnitudes corresponding to data from the Rubin Observatory ($m_{\rm RO}^{\rm lim}$) are also listed.

binary evolution via the CE phase. As discussed in Section 3.2, by leveraging the BHNS binary population-synthesis model from F. S. Broekgaarden et al. (2021), we present compelling evidence that the system's properties are consistent with the predictions derived from the isolated binary evolution pathway of BHNS systems. However, due to the event's relatively low SNR, we face difficulties in identifying the underlying physical mechanism driving its formation unequivocally. However, we could rule out with confidence certain formation mechanisms such as the one involving the "rapid SNe" or the "unstable case BB."

Using our posterior samples and numerical fits from F. Zappa et al. (2019) and A. Gonzalez et al. (2023), we infer the remnant's mass and spin, finding that it is consistent with a BH with $M_f \sim 5.3\,M_\odot$ and $\chi_f \sim 0.53$. We also predict that there is a $\gtrsim$99% probability that NS is tidally disrupted during the merger and about a 13% probability that such disruption occurs outside $R_{\rm ISCO}$, leading to potential electromagnetic counterparts and a suppressed ringdown signal.

We compute KN light curves using our population-informed posterior samples and the isotropic framework proposed by W. D. Arnett (1980), D. Arnett (1982), E. Chatzopoulos et al. (2012), and V. A. Villar et al. (2017). We find that the i-band luminosity is dim enough not to be observed in a regular Rubin search but may be bright enough to be observed in a targeted one.

Overall, GW230529 is a notable addition to the growing population of compact binaries observed in the GW window. It marks the first of many more events with components with masses between $\sim$3 and 5 $M_\odot$, the so-called "lower mass gap" that divides the NS and BH populations.

Acknowledgments

We thank Simon Stevenson and Aditya Vijaykumar for their comments and valuable suggestions. K.C., I.G., R.K., and B.S. S. acknowledge the support through NSF grant Nos. PHY-2207638, AST-2307147, PHY-2308886, and PHY-2309064. R.G. acknowledges support from NSF grant PHY-2020275 (Network for Neutrinos, Nuclear Astrophysics, and Symmetries (N3AS)). D.C. is supported by the STFC grant ST/V005618/1. S.B. acknowledges funding from the EU Horizon under ERC Consolidator grant No. InspiReM-101043372. D.C. and B.S.S. thank the Aspen Center for Physics (ACP) summer workshop 2022 for setting up discussions that also contributed to this collaborative work. TEOBResumS is publicly available at https://bitbucket.org/eob_ihes/teobresums. The version employed in this work is tagged via the arXiv submission number of the paper itself. This research has made use of data, software, and/or web tools obtained from the Gravitational Wave Open Science Center (https://www.gw-openscience.org), a service of LIGO Laboratory, the LIGO Scientific Collaboration, the Virgo Collaboration, and KAGRA. This material is based upon work supported by NSF's LIGO Laboratory, which is a major facility fully funded by the National Science Foundation. LIGO Laboratory and Advanced LIGO are funded by the United States National Science Foundation (NSF) as well as the Science and Technology Facilities Council (STFC) of the United Kingdom, the Max-Planck-Society (MPS), and the State of Niedersachsen/Germany for support of the construction of Advanced LIGO and construction and operation of the GEO600 detector. Additional support for Advanced LIGO was provided by the Australian Research Council. Virgo is funded through the European Gravitational Observatory (EGO), the French Centre National de Recherche Scientifique (CNRS), the Italian Istituto Nazionale di Fisica Nucleare (INFN), and the Dutch Nikhef, with contributions by institutions from Belgium, Germany, Greece, Hungary, Ireland, Japan, Monaco, Poland, Portugal, and Spain. KAGRA is supported by the Ministry of Education, Culture, Sports, Science and Technology (MEXT), Japan Society for the Promotion of Science (JSPS) in Japan; National Research Foundation (NRF) and Ministry of Science and ICT (MSIT) in Republic of Korea; and Academia Sinica (AS) and National Science and Technology Council (NSTC) in Taiwan. This document has been assigned the LIGO document number LIGO-P2400163.

Appendix A
Waveform Systematics

LVK demonstrated that while they are not dominant with respect to statistical uncertainties, systematic errors due to the choice of the employed GW models are not negligible. Moreover, GW230529 inhabits a parameter space previously unexplored through observations. In this appendix, we elucidate that systematic uncertainties hold minimal significance within the framework of population-informed priors. Furthermore, we assert that the findings presented in this study remain robust regardless of the specific model chosen.

To substantiate this claim, we perform the following analyses. (i) We measure the mismatch between the two waveform models, namely IMRPhenomNSBH and TEOBResumS-GIOTTO (S. Akcay et al. 2019; A. Nagar et al. 2020a, 2020b; A. Gonzalez et al. 2023)—the latter being an effective-one-body model for compact objects informed by NR simulations of merging binary BHs and BHNS systems containing higher modes and tidal disruption (A. Buonanno & T. Damour 1999). This study uses posterior samples obtained when assuming the fiducial model. (ii) We assess the robustness of mass-parameter measurements against modeling systematics when employing the aforementioned waveform models.

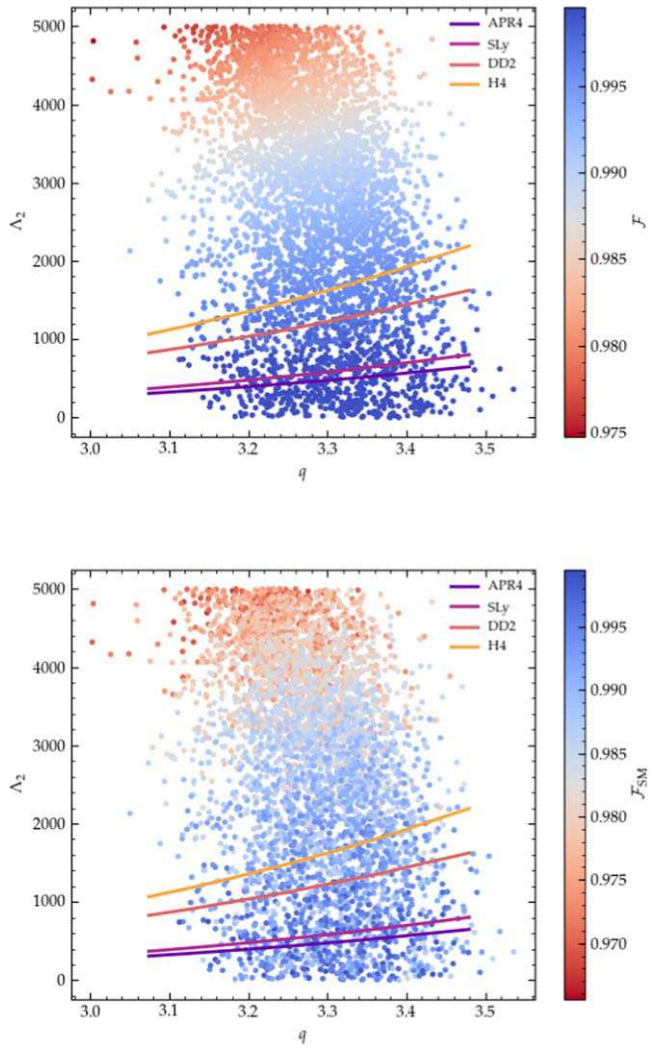

Figure 8. Match $\mathcal{F}$ and sky-maximized match $\mathcal{F}_{\rm SM}$ between polarizations constructed using the dominant quadrupolar (top) and subdominant (bottom) modes of `TEOBResumS-GIOTTO` and `IMRPhenomNSBH`. We consider posterior samples from the fiducial PE and compute $\mathcal{F}$ between 20 and 1796 Hz. Depending on whether higher modes are employed or not, we find median mismatches of about $\sim$1.4% (0.8%) and maximum mismatches of $\sim$3% ($\sim$2%), corresponding to systems with large tidal parameters $\Lambda_2 > 3000$. Overlaid, we also plot the tidal parameters obtained with a few selected EOSs, assuming a fixed BH source-frame mass of 4.2 $M_\odot$.

A.1. Comparison between `TEOBResumS-GIOTTO` and `IMRPhenomNSBH`

We quantify the discrepancy between the waveform models in terms of the match (or faithfulness; C. Cutler & E. E. Flanagan 1994; T. A. Apostolatos 1995):

$$\mathcal{F} = \max_{t_{\rm ref},\phi_{\rm ref}} \frac{(h|k)}{\sqrt{(h|h)(k|k)}}, \tag{A1}$$

where $t_{\rm ref}$ and $\phi_{\rm ref}$ are a reference time and phase, h and k are the two waveforms considered and

$$(h|k) = 4\Re \int_{f_{\rm min}}^{f_{\rm max}} \frac{\tilde{h}(f)\tilde{k}^*(f)}{S_n(f)} df. \tag{A2}$$

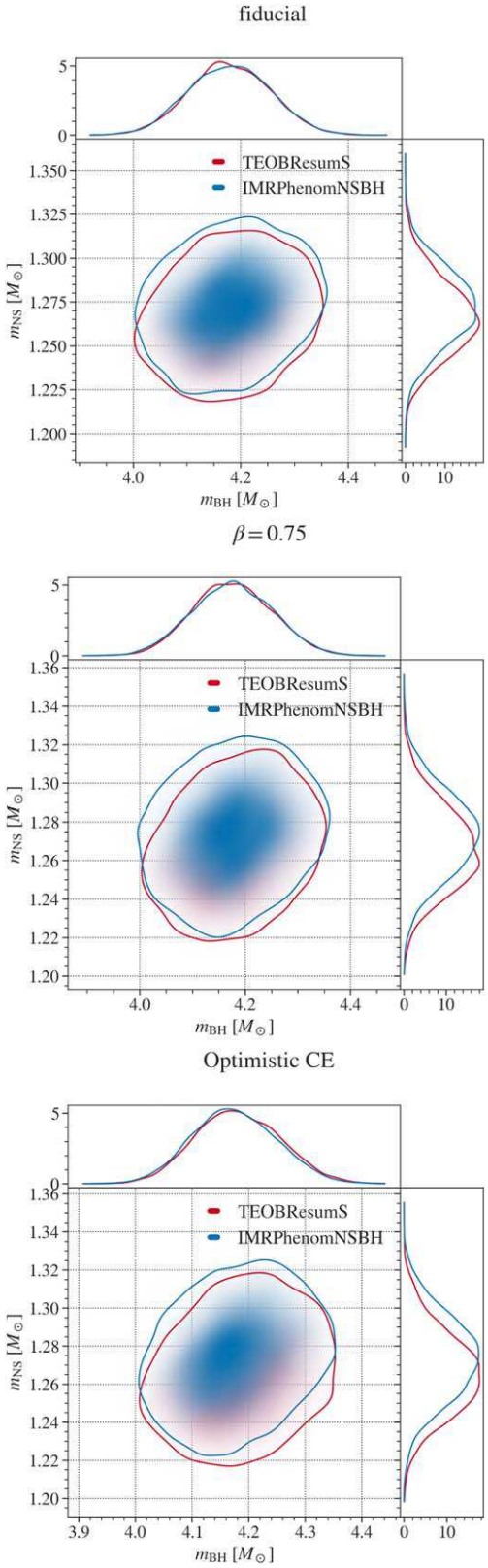

Figure 9. The posterior distribution of the primary and secondary source masses for two different waveform models—`TEOBResumS-GIOTTO` and `IMRPhenomNSBH`. Each contour shows the 90% credible intervals. We find that the resulting parameter estimates are robust to possible waveform systematics, with good agreement between the two waveform models.

Since TEOBResumS-GIOTTO contains higher-order radiation multipoles,[6] the definition above is not independent of the extrinsic parameters of the binary. We therefore maximize over the sky position and polarization by computing the sky-maximized match $\mathcal{F}_{\rm SM}$ as defined in I. Harry et al. (2018) and K. Chandra et al. (2022). This statistic reduces to Equation (A1) when only (2, |2|) modes are employed. We then compute this quantity over the frequency interval [20, 1796] Hz and employ the power spectral density S_n of GW230529. Crucially, to avoid noise artifacts in the fast Fourier transform, we generate the waveforms from 18 Hz and taper them at the beginning.

We find that the mismatches always lie below the 2.5% threshold when only (2, |2|) modes are considered and below 3.5% when subdominant multipoles are included in the polarization computation (see Figure 8). As expected, both $\mathcal{F}$ and $\mathcal{F}_{\rm SM}$ decrease with increasing tidal parameters: if one reduces the interval of Λ_2 considered to [0, 3000], the maximum values for the figures above shift to 1.2% and 2.3%, respectively. This is because NSs characterized by large values of Λ_2 are more easily disrupted, leading to growing differences in the model's predictions in a region poorly explored by NR simulations.

To understand whether the matches obtained are "acceptable," they should, in principle, be compared to some accuracy requirement, i.e., to some theoretical threshold below which one may expect waveform systematics to appear (C. Cutler & E. E. Flanagan 1994; L. Lindblom et al. 2008; T. Damour et al. 2011; K. Chatziioannou et al. 2017; A. Toubiana & J. R. Gair 2024). While correctly assessing accuracy requirements is largely a back-of-the-envelope estimate can be obtained employing the following threshold $\mathcal{F}_{\rm thrs}$ (T. Damour et al. 2011; K. Chatziioannou et al. 2017):

$$\mathcal{F}_{\rm thrs} = 1 - \frac{\epsilon}{2\rho^2}, \tag{A3}$$

where ϵ is the number of intrinsic parameters of the system. This choice leads to $\mathcal{F}_{\rm thrs} = 0.988$ ($\epsilon = 3$), smaller than ∼65% of the matches computed when only (2, |2|) modes are considered. When subdominant modes are further included in the analysis, inclination should be treated as an intrinsic source parameter and $\mathcal{F}_{\rm thrs} = 0.984$, smaller than 58% of the mismatches computed. As such, though some differences between models are certainly present, one should not expect large biases to appear.

A.2. Reanalysis with TEOBResumS

We repeated some of the population-informed PEs using the time-domain waveform model TEOBResumS-GIOTTO, as shown in Figure 9. The results indicate that the GW230529's source-mass parameters are robust against modeling systematics. This is consistent with the faithfulness study performed in the previous section. Although the models employ entirely independent descriptions of both point-mass and tidal sectors, differences are largely irrelevant: the high-frequency component of the data is dominated by noise and, as such, does not affect the inference. Additionally, our prior constrains the spins of the system components to be effectively zero, further minimizing the differences between models.

Appendix B
Kilonova Light Curves

As noted in Section 4.3, the KN light curves were generated using numerical recipes in I. Gupta et al. (2023). We only consider samples where the mass ratio is less than 4. We assume the electron fraction for the dynamical ejecta to be 0.1 and for the unbound disk ejecta to be 0.3 (N. Ekanger et al. 2023). The opacity values are obtained by fitting to data from M. Tanaka et al. (2020).

The four chosen EOSs in Section 4.3 span a wide range in the mass–radius diagram (see Figure 10). This allows us to gauge the effect of different nuclear-matter compositions on the expected electromagnetic counterpart. Notably, the BSK24 EOS (S. Goriely et al. 2013)—used by LVK —is contained within this range. Figure 11 shows the results corresponding to the DD2 EOS, which show similar features to those from H4.

To compare our results with J.-P. Zhu et al. (2024), in Figure 12 we show the distribution of the peak luminosity in the g and r bands for the "fiducial" model and the DD2 EOS. While the two works get similar estimates for peak luminosities, our model results in dimmer KNe compared to the one used by J.-P. Zhu et al. (2024). Furthermore, the maximum-likelihood binary parameters correspond to a significantly fainter KN, affecting the KN's detectability from such systems.

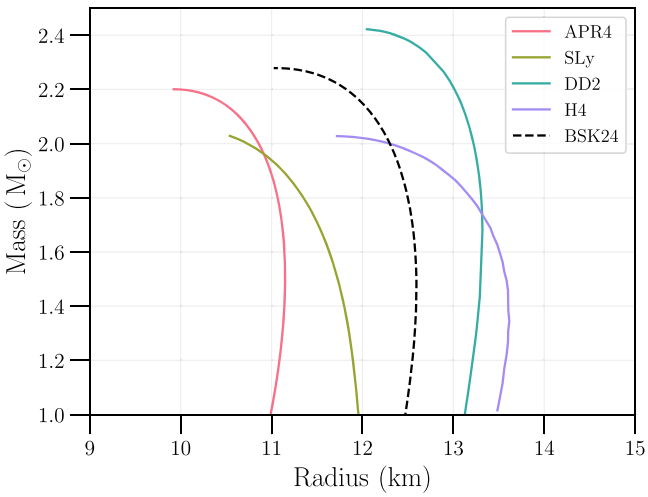

Figure 10. The mass–radius curves for the EOSs chosen in this study. We also show the BSK24 EOS, which was used by LVK.

[6] In detail, we employ the $(\ell, |m|) = (2, 1), (2, 2), (3, 3), (4, 4)$ modes.

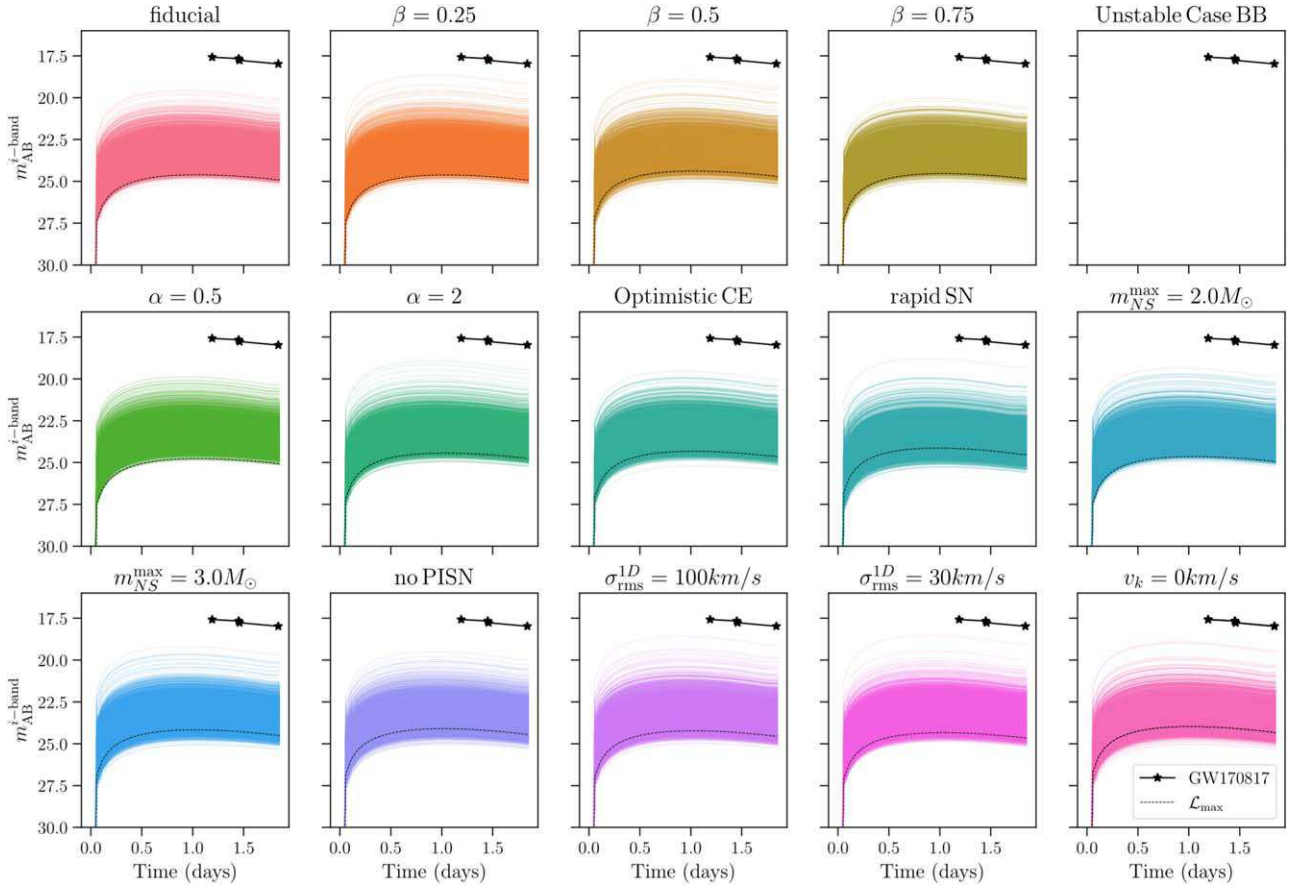

Figure 11. KN light curves in the *i* band corresponding to the different population models for the DD2 EOS. The dotted line shows the light curve associated with the maximum-likelihood parameter estimates for each model.

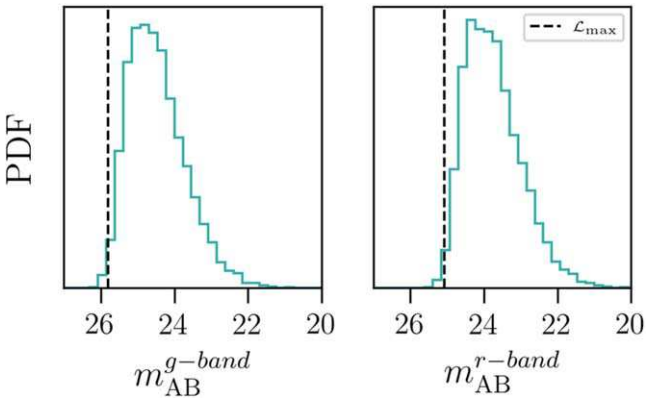

Figure 12. The distribution of the peak luminosity in the *g* and *r* bands for the DD2 EOS corresponding to samples from the "fiducial" population model. The black dotted line shows the peak luminosity corresponding to the maximum-likelihood binary parameters.

ORCID iDs

Koustav Chandra https://orcid.org/0000-0003-4750-5551
Ish Gupta https://orcid.org/0000-0001-6932-8715
Rossella Gamba https://orcid.org/0000-0001-7239-0659
Rahul Kashyap https://orcid.org/0000-0002-5700-282X
Debatri Chattopadhyay https://orcid.org/0000-0001-5867-5033
Alejandra Gonzalez https://orcid.org/0000-0002-5034-9353
Sebastiano Bernuzzi https://orcid.org/0000-0002-2334-0935
B. S. Sathyaprakash https://orcid.org/0000-0003-3845-7586

References

Aasi, J., Abadie, J., Abbott, B. P., et al. 2015, CQGra, 32, 074001
Abbott, B. P., Abbott, R., Abbott, T. D., et al. 2017, PhRvL, 119, 161101
Abbott, B. P., Abbott, R., Abbott, T. D., et al. 2019a, PhRvX, 9, 031040
Abbott, B. P., Abbott, R., Abbott, T. D., et al. 2019b, PhRvX, 9, 011001
Abbott, R., Abbott, T. D., Abraham, S., et al. 2021, PhRvX, 11, 021053
Akcay, S., Bernuzzi, S., Messina, F., et al. 2019, PhRvD, 99, 044051
Akmal, A., Pandharipande, V. R., & Ravenhall, D. G. 1998, PhRvC, 58, 1804
Alsing, J., Silva, H. O., & Berti, E. 2018, MNRAS, 478, 1377
Antoniadis, J., Tauris, T. M., Ozel, F., et al. 2016, arXiv:1605.01665
Apostolatos, T. A. 1995, PhRvD, 52, 605
Arnett, D. 1982, ApJ, 253, 785
Arnett, W. D. 1980, ApJ, 237, 541
Ashton, G., & Dietrich, T. 2022, NatAs, 6, 961
Ashton, G., Hubner, M., Lasky, P. D., et al. 2019, ApJS, 241, 27
Bailyn, C. D., Jain, R. K., Coppi, P., & Orosz, J. A. 1998, ApJ, 499, 367
Barbieri, C., Salafia, O. S., Colpi, M., et al. 2019, ApJL, 887, L35
Barbieri, C., Salafia, O. S., Perego, A., Colpi, M., & Ghirlanda, G. 2020, EPJA, 56, 8
Bavera, S. S., Fragos, T., Qin, Y., et al. 2020, A&A, 635, A97
Belczynski, K., Bulik, T., Fryer, C. L., et al. 2010, ApJ, 714, 1217
Belczynski, K., Romagnolo, A., Olejak, A., et al. 2022, ApJ, 925, 69
Biscoveanu, S., Landry, P., & Vitale, S. 2022, MNRAS, 518, 5298
Branchesi, M., Maggiore, M., Alonso, D., et al. 2023, JCAP, 07, 068
Breschi, M., Gamba, R., Carullo, G., et al. 2024, A&A, 689, A51
Broekgaarden, F. S., & Berger, E. 2021, ApJL, 920, L13
Broekgaarden, F. S., Berger, E., Neijssel, C. J., et al. 2021, MNRAS, 508, 5028
Buonanno, A., & Damour, T. 1999, PhRvD, 59, 084006
Chabanat, E., Bonche, P., Haensel, P., Meyer, J., & Schaeffer, R. 1998, NuPhA, 635, 231
Chandra, K., Calderón Bustillo, J. C., Pai, A., & Harry, I. W. 2022, PhRvD, 106, 123003
Chattopadhyay, D., Stevenson, S., Broekgaarden, F., Antonini, F., & Belczynski, K. 2022, MNRAS, 513, 5780

Chattopadhyay, D., Stevenson, S., Hurley, J. R., Bailes, M., & Broekgaarden, F. 2021, MNRAS, 504, 3682
Chatziioannou, K., Klein, A., Yunes, N., & Cornish, N. 2017, PhRvD, 95, 104004
Chatzopoulos, E., Craig Wheeler, J., & Vinko, J. 2012, ApJ, 746, 121
Cornish, N. J. 2010, arXiv:1007.4820
Cornish, N. J. 2021, PhRvD, 104, 104054
Cutler, C., & Flanagan, E. E. 1994, PhRvD, 49, 2658
Damour, T., Nagar, A., & Trias, M. 2011, PhRvD, 83, 024006
Dietrich, T., Samajdar, A., Khan, S., et al. 2019, PhRvD, 100, 044003
Douchin, F., & Haensel, P. 2001, A&A, 380, 151
Ekanger, N., Bhattacharya, M., & Horiuchi, S. 2023, MNRAS, 525, 2040
Farah, A., Fishbach, M., Essick, R., Holz, D. E., & Galaudage, S. 2022, ApJ, 931, 108
Farr, W. M., & Chatziioannou, K. 2020, RNAAS, 4, 65
Farr, W. M., Sravan, N., Cantrell, A., et al. 2011, ApJ, 741, 103
Fishbach, M., Essick, R., & Holz, D. E. 2020, ApJL, 899, L8
Fonseca, E., Cromartie, H. T., Pennucci, T. T., et al. 2021, ApJL, 915, L12
Foucart, F., Buchman, L., Duez, M. D., et al. 2013, PhRvD, 88, 064017
Foucart, F., Deaton, M. B., Duez, M. D., et al. 2014, PhRvD, 90, 024026
Fragos, T., & McClintock, J. E. 2015, ApJ, 800, 17
Fryer, C. L., Belczynski, K., Wiktorowicz, G., et al. 2012, ApJ, 749, 91
Garcia, A. M., Torrey, P., Ellison, S., et al. 2024, MNRAS, 531, 1398
Glendenning, N., & Moszkowski, S. 1991, PhRvL, 67, 2414
Godzieba, D. A., Radice, D., & Bernuzzi, S. 2021, ApJ, 908, 122
Gonzalez, A., Gamba, R., Breschi, M., et al. 2023, PhRvD, 107, 084026
Goriely, S., Chamel, N., & Pearson, J. M. 2013, PhRvC, 88, 061302
Guillochon, J., Parrent, J., Kelley, L. Z., & Margutti, R. 2017, ApJ, 835, 64
Gupta, I. 2023, MNRAS, 524, 3537
Gupta, I. 2024, ApJ, 970, 12
Gupta, I., Borhanian, S., Dhani, A., et al. 2023, PhRvD, 107, 124007
Harry, I., Calderón Bustillo, J. C., & Nitz, A. 2018, PhRvD, 97, 023004
Hempel, M., & Schaffner-Bielich, J. 2010, NuPhA, 837, 210
Hurley, J. R., Pols, O. R., & Tout, C. A. 2000, MNRAS, 315, 543
Ivanova, N., Justham, S., Chen, X., et al. 2013, A&ARv, 21, 59
Ivezić, Z., et al. 2019, ApJ, 873, 111
Kashyap, R., Raman, G., & Ajith, P. 2019, ApJ, 886, L19
Kawaguchi, K., Domoto, N., Fujibayashi, S., et al. 2024, arXiv:2404.15027
Khan, S., Husa, S., Hannam, M., et al. 2016, PhRvD, 93, 044007
Krishna, K., Vijaykumar, A., Ganguly, A., et al. 2023, arXiv:2312.06009
Krüger, C. J., & Foucart, F. 2020a, PhRvD, 101, 103002
Krüger, C. J., & Foucart, F. 2020b, PhRvD, 101, 103002
Kyutoku, K., Kiuchi, K., Sekiguchi, Y., Shibata, M., & Taniguchi, K. 2018, PhRvD, 97, 023009
Kyutoku, K., Shibata, M., & Taniguchi, K. 2021, LRR, 24, 5
Lackey, B. D., Nayyar, M., & Owen, B. J. 2006, PhRvD, 73, 024021
Langeroodi, D., Hjorth, J., Chen, W., et al. 2023, ApJ, 957, 39
Lattimer, J. M., & Schramm, D. N. 1974, ApJ, 192, L145
Lattimer, J. M., & Schramm, D. N. 1976, ApJ, 210, 549
Ligo Scientific Collaboration, VIRGO Collaboration, & Kagra Collaboration 2024, ApJL, 970, L34
Lindblom, L., Owen, B. J., & Brown, D. A. 2008, PhRvD, 78, 124020
Littenberg, T. B., & Cornish, N. J. 2015, PhRvD, 91, 084034
Ma, L., & Fuller, J. 2019, MNRAS, 488, 4338
Mandel, I., & Broekgaarden, F. S. 2022, LRR, 25, 1
Mandel, I., & Fragos, T. 2020, ApJL, 895, L28
Metzger, B. D. 2017, LRR, 20, 3
Miller, M. C., Lamb, F. K., Dittmann, A. J., et al. 2021, ApJL, 918, L28
Nagar, A., Pratten, G., Riemenschneider, G., & Gamba, R. 2020a, PhRvD, 101, 024041
Nagar, A., Riemenschneider, G., Pratten, G., Rettegno, P., & Messina, F. 2020b, PhRvD, 102, 024077
Ozel, F., Psaltis, D., Narayan, R., & McClintock, J. E. 2010, ApJ, 725, 1918
Qin, Y., Fragos, T., Meynet, G., et al. 2018, A&A, 616, A28
Raaijmakers, G., Nissanke, S., Foucart, F., et al. 2021, ApJ, 922, 269
Ray, A., Magaña Hernandez, I. M., Mohite, S., Creighton, J., & Kapadia, S. 2023, ApJ, 957, 37
Read, J. S., Lackey, B. D., Owen, B. J., & Friedman, J. L. 2009, PhRvD, 79, 124032
Romani, R. W., Kandel, D., Filippenko, A. V., Brink, T. G., & Zheng, W. 2022, ApJL, 934, L17
Speagle, J. S. 2020, MNRAS, 493, 3132
Tanaka, M., Kato, D., Gaigalas, G., & Kawaguchi, K. 2020, MNRAS, 496, 1369
Thompson, J. E., Fauchon-Jones, E., Khan, S., et al. 2020, PhRvD, 101, 124059
Thrane, E., & Talbot, C. 2019, PASA, 36, e010
Toubiana, A., & Gair, J. R. 2024, arXiv:2401.06845
Typel, S., Ropke, G., Klahn, T., Blaschke, D., & Wolter, H. H. 2010, PhRvC, 81, 015803
Veitch, J., & Vecchio, A. 2010, PhRvD, 81, 062003
Villar, V. A., Guillochon, J., Berger, E., et al. 2017, ApJL, 851, L21
Vinciguerra, S., Salmi, T., Watts, A. L., et al. 2024, ApJ, 961, 62
Zackay, B., Dai, L., & Venumadhav, T. 2018, arXiv:1806.08792
Zappa, F., Bernuzzi, S., Pannarale, F., Mapelli, M., & Giacobbo, N. 2019, PhRvL, 123, 041102
Zhu, J.-P., Hu, R.-C., Kang, Y., et al. 2024, ApJ, 974, 211